Research Article | Vol. 29, No. 3 / 1 February 2021 / Optics Express 4296
Optics EXPRESS

Femtosecond laser direct writing of depressed cladding waveguides in Nd:YAG with "ear-like" structures: fabrication and laser generation

XIAOLI SUN,[1] SHUO SUN,[1] CAROLINA ROMERO,[2] JAVIER R. VÁZQUEZ DE ALDANA,[2] FENGQIN LIU,[1] YUECHEN JIA,[1,3] AND FENG CHEN[1,4]

[1]School of Physics, State Key Laboratory of Crystal Materials, Shandong University, Jinan 250100, China
[2]Grupo de investigación en Aplicaciones del Láser y Fotónica, Universidad de Salamanca, Salamanca 37008, Spain
[3]yuechen.jia@sdu.edu.cn
[4]drfchen@sdu.edu.cn

Abstract: Low-loss depressed cladding waveguide architecture is highly attractive for improving the laser performance of waveguide lasers. We report on the design and fabrication of the "ear-like" waveguide structures formed by a set of parallel tracks in neodymium-doped yttrium aluminum garnet (Nd:YAG) crystal via femtosecond laser writing. The obtained "ear-like" waveguides are with more symmetric mode profiles and lower losses by systematically comparing the guiding properties of two kinds of normal cladding waveguide. Efficient waveguide lasers are realized based on the designed structure in both continuous wave and pulsed regimes. Combined the high-gain from cladding waveguide and special "ear-like" structure, a passively fundamentally Q-switched laser with the narrow pulse width and the high repetition rate has been obtained by using tin diselenide ($SnSe_2$) as saturable absorber.

1. Introduction

Optical waveguides are far more than merely connecting elements between integrated optical components. Benefiting from their strong optical confinement, dielectric waveguides are full of possibilities for functional optical devices as well [1–4]. Solid-state channel waveguide lasers are among the most promising architectures for compact and robust laser sources because they are able to offer enhanced optical gain, reduced lasing threshold, and miniaturized footprints [5–10]. Femtosecond laser direct writing (FsLDW), which is a rapidly evolving technology, exploits tightly focused femtosecond laser pulses to modify the optical properties of a small volume inside a transparent material, inducing localized and controllable refractive index modification in a direct procedure without using any patterned masking [11]. Such a technology therefore allows monolithic and sophisticated waveguide fabrication in a very flexible manner [12]. In addition, FsLDW exhibits good compatibility to a broad range of crystal families, providing a promising avenue for constructing multifunctional optical devices towards 3D integrated photonic [13–16]. The most commonly used morphological geometries of waveguides defined by FsLDW are characterized as tunnel-like "single-line" (based on Type-I modification), stress-field induced "double-line" (based on Type-II modification), and fiber-like "depressed-cladding" (based on Type-II modification) structures [10,17,18].

Depressed-cladding waveguide is consisted of a guiding core surrounded by a number of low-index laser tracks [19–21]. Those laser tracks are close to each other (few micrometers), constructing a quasi-continuous low-index potential barrier wall, providing the required optical confinement [22,23]. However, the roughness of laser tracks defined by FsLDW usually act as scatters, which is the primary origin of optical loss for FsDLW waveguides [22]. Actually,

#417815 https://doi.org/10.1364/OE.417815
Journal © 2021 Received 17 Dec 2020; revised 19 Jan 2021; accepted 20 Jan 2021; published 26 Jan 2021

Optics EXPRESS

the impact from imperfect boundary on optical guiding can be lowered by adding additional layer of laser-induced low-index tracks. For example, it has been found that the double-cladding waveguide structures and the photonic-lattice-like cladding photonic structures (usually with multi-layer of low-index laser tracks) defined by FsDLW exhibit good optical confinement and reduced waveguide loss in comparison to their standard single-cladding (also called depressed cladding) waveguides [24]. However, the introduction of an additional layer (or multi-layer) of laser tracks in the abovementioned structures will significantly increase the whole size and the fabrication period of waveguide structures. A smarter and less time-consuming procedure is necessary. In this work we investigate the properties of depressed-cladding waveguide geometry with an "ear-like" structure, in order to enhance the optical confinement of light field. This design is an evolved scheme of the solution firstly presented by Okhrimchuk et al. [22], the present approach being based on a smart combination of the standard FsLDW double-line and depressed cladding waveguides.

Low-dimensional materials possess intriguing and novel optoelectronic nature, which enable a fresh class of photonics devices, paving the way for nanomaterials integrated with waveguides [25–29]. Tin diselenide ($SnSe_2$), a novel member of the transitional metal dichalcogenides (TMDs) family, is a narrow bandgap semiconductor with the hexagonal structure. Like other TMDs materials, the band structure of $SnSe_2$ is relative to the thickness of the nanosheets, from 1.07 eV for bulk to 1.69 eV for monolayer [30]. As previous reported, the nonlinear coefficient β_{eff} is about 10^4 cm/GW [31], which is similar to that of Graphene-Bi_2Te_3 heterostructure and is six orders of magnitude higher than those of TMDs MoS_2 and $MoSe_2$ [32,33], indicating a strong optical switch capability. On the basis of the effective mass and carrier mobility, the relaxation time for the electrons and holes of monolayer $SnSe_2$ is 186 and 135 fs, respectively [34]. All above properties make $SnSe_2$ a promising infrared optoelectronic device for the applications of ultrafast photonics.

In this work, we design four types cladding ring with extra lines of tracks at the sides ("ear-like" structure) which aim to "strength" the cladding wall by femtosecond direct writing, and investigate the guiding properties and mode profiles at 1064 nm. Compared with the single-cladding waveguide, the cladding with "ear-like" structure has a lower laser threshold, higher output power and beam quality. Using $SnSe_2$ nanosheets as saturable absorber (SA), a nanosecond pulsed operation with duration as short as 40.3 ns is realized. To the best of our knowledge, this pulse duration is the shortest ever reported for passive Q-switched bulk lasers based on $SnSe_2$ SA.

2. Sample preparation

2.1. Depressed cladding waveguide fabrication

The raw Nd:YAG (1 at.% Nd^{3+} ions) crystal wafer used in this work has dimensions of $20 \times 10 \times 2$ mm^3. All the crystal facets have been well polished to optical grade. A Ti:Sapphire regenerative amplifier (Spitfire, Spectra Physics), which delivers 795 nm pulses with a temporal duration of 120 fs and a maximum pulse energy of 1 mJ at a repetition rate of 1 kHz, is employed to fabricate cladding structures buried inside the crystal wafer. In the laser-writing process shown as Fig. 1(a), the incident laser beam is focused through the largest crystal facet ($20 \times 2mm^2$) at a maximum depth of 150 μm by a 50× microscope objective (N.A. = 0.65). The crystal wafer is placed on a motorized XYZ micro-positioning stage which allows for precise translation of the sample at a constant velocity (0.5 mm/s in this work to minimize the stress effect induced by laser pulses) with respect to the incident laser beam. A pulse energy of 0.33 μJ (on sample) is identified as the optimal value in order to produce laser-damage tracks while avoiding crystal cracking. Under our experimental conditions, a damage track with a vertical length of 5 μm and a lateral width of 1.5 μm can be produced via a single scan. A number of parallel scans are performed, with a constant lateral separation of 3 μm, at different depths beneath the crystal surface to define the

Optics EXPRESS

desired cladding structures: four single-cladding waveguides with radii of 10 (WG1), 15 (WG2), 20 (WG3) and 25 μm (WG4), respectively, and four corresponding claddings with "ear-like" structures (namely, WG1e-WG4e). Figure 1(b) shows the optical microscope cross-sectional images of the fabricated waveguides. The definition of such an "ear-like" structure is intended to further enhance the optical confinement along TM polarization while maintaining the lasing performance along TE polarization, which is a fairly straightforward approach borrowed from the so-called "double-line" waveguides fabricated by FsLDW [35]. In "double-line" structures, usually, low-loss waveguiding and efficient lasing occur along only TM polarization, *i.e.*, along the orientation parallel to FsLDW tracks, as a result of the anisotropy in both waveguide geometry and stress-field-induced refractive index profile. All the waveguides are written along the 10-mm length of the crystal wafer. The end-facets are kept uncoated, as shown in Fig. 1(b).

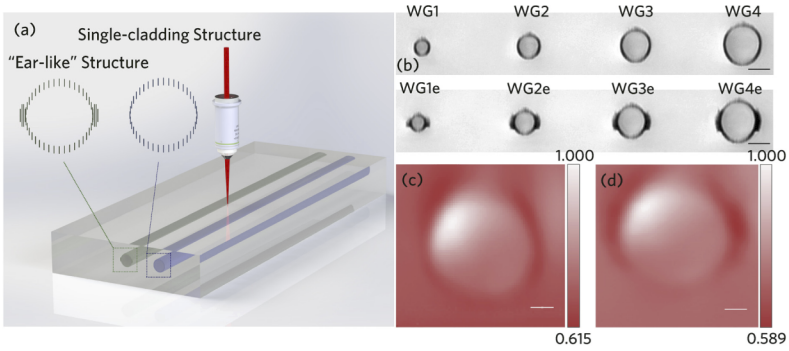

Fig. 1. (a) Schematic plot of the single-cladding and "ear-like" waveguides. (b) Optical microscope cross-sectional image of single-cladding waveguides (WG1-WG4) and "ear-like" claddings (WG1e-WG4e) with different radius of 10 μm, 15 μm, 20 μm, and 25 μm, respectively. scale bar denotes 30 μm. Micro-photoluminescence measurements. The spatial distributions of emitted intensity obtained from the WG4 (c) and WG4e (d).

2.2. $SnSe_2$ thin film characterization

The $SnSe_2$ sample (a commercial product provided by 6Carbon Technology, China) is customized to be a multi-layer thin film deposited on a sapphire substrate (with a surface area of 10 mm × 10 mm) via chemical vapor deposition (CVD). The atomic force microscopy (AFM) measurement operating in the tapping mode (lessen the damage done to the thin film surface) is carried out with a view to investigating the surface morphology and the thickness of the deposited $SnSe_2$ thin film. In order to verify the thickness of $SnSe_2$ sheets, we select an area in where the film is broken. Figure 2(a) is the acquired AFM topological image, revealing the good homogeneity of the as-deposited sample. The dark areas in the middle indicate the position without sample. The bright areas on both sides indicate the $SnSe_2$ flakes. The thickness of the $SnSe_2$ thin film is determined to be 9 nm from Fig. 2(a), as confirmed by the measured height profile. The Raman spectrum (to examine the composition-dependent vibration modes) of $SnSe_2$ is shown in Fig. 2(b), indicating two prominent vibration peaks assigned to characteristic A_{1g} mode (out-of-plane vibrational mode) at 184.9 cm^{-1} and E_g mode (in-plane vibrational mode) at 118.3 cm^{-1}, which is fairly consistent with the results in previous reports [36]. The linear optical absorption properties of the $SnSe_2$ sample over the visible to the near-infrared is investigated by a UV/VIS/NIR spectrophotometer (U-3500 HITACHI), as shown in Fig. 3. The absorbance of $SnSe_2$ SA at 1064 nm is measured to be about 0.307, which has subtracted the Fresnel reflection loss of the sapphire substrate.

Optics EXPRESS

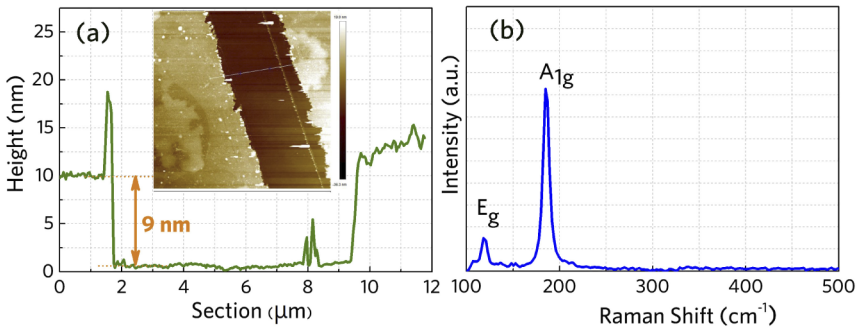

Fig. 2. (a) AFM image of $SnSe_2$ SA. Inset: the corresponding height profiles of the section marked in AFM. (b) Raman spectra and characteristic Raman peaks.

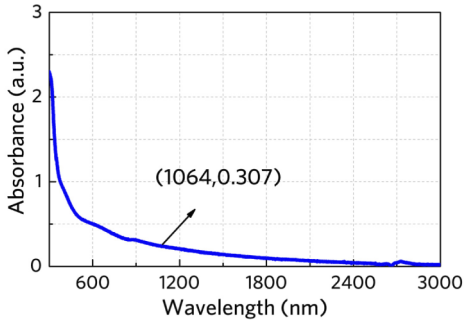

Fig. 3. Absorbance spectra of the few-layered $SnSe_2$ nanosheets.

In order to investigate the saturable absorption property as well as to testify the potential application of the prepared $SnSe_2$ thin film for 1-μm ultrafast laser generation, we use the open-aperture z-scan technique. In this setup, a femtosecond ytterbium fiber laser (FemtoYL-10, YSL Photonics, China), which delivers 1035 nm pulses with a temporal duration of 400 fs and a maximum pulse energy of 400 μJ at a tunable repetition rate of 25 kHz-5 MHz, is used as the excitation source. The beam waist radius of the laser beam focused on the $SnSe_2$ sample is around 52 μm, reaching a sufficient high intensity for optical excitation while assuring that the sample is free of laser-induced damage. During the z-scan measurement, the $SnSe_2$ sample is placed on a PC-controlled translation stage and moved through the focus of the laser beam (z direction), experiencing continuously varied laser intensities at non-focus and on-focus positions. While moving the sample, the real-time powers of the reference and transmitted light are detected.

Figure 4(a) demonstrates the normalized transmittance as a function of the sample position, exhibiting a typical nonlinear absorption curve with a good symmetry at the $z = 0$ position (the excitation pulse energy is attenuated to 10 μJ by an attenuation slice and the repetition rate is set be 25 kHz in order to weaken the thermal effect). Such a z-scan curve with a sharp and narrow peak at the focus position confirms the valid saturable absorption property (at 1035 nm) of the $SnSe_2$ sample used in this work. In order to obtain more detailed information of the saturation fluence and modulation depth, the experimental data is fitted with the nonlinear absorption model using the following formula [37],

$$T = [1 - \frac{\eta I_s}{I_s + \frac{I_0}{1+\frac{z^2}{z_0^2}}}]/(1-\eta) \tag{1}$$

Optics EXPRESS

where T represents the normalized transmittance, η is the modulation depth, I_0 and I_s represent the incident peak intensity and saturation intensity, respectively. z_0 means the Rayleigh length of beam. With the single-photon absorption model, the saturation fluence and modulation depth of the $SnSe_2$ thin film is determined to 64 μJ/cm^2 and 3.26%, respectively. The non-saturable loss is about 23%, which may be caused by the surface scattering, absorption of defects and impurities. Higher non-saturable loss leads to the reduction in output power. As the incident intensity increased, the saturable absorption parameters are constant. To further verify the nonlinear optical response, we also measure the transmittance variation of the $SnSe_2$ sample as a function of the incident femtosecond laser intensity presented in the inset of Fig. 4(b), indicating the optical absorption of the $SnSe_2$ sample tending to be saturated with the increase of the incident laser intensity at 1035 nm (considering the Gaussian distribution of the laser beam).

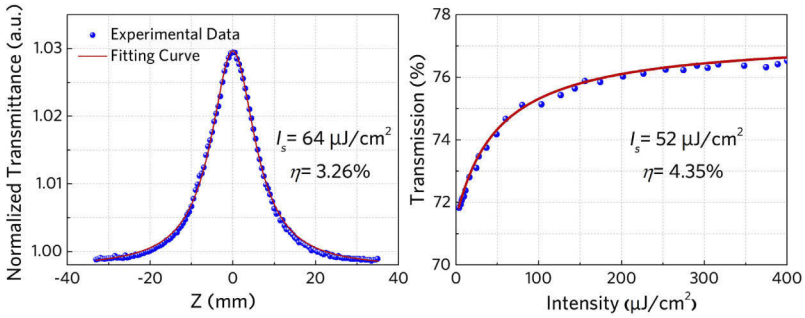

Fig. 4. (a) The open aperture Z-scan characterization. (b) The nonlinear transmittance curves of $SnSe_2$ SA.

3. Optical characterization

3.1. Passive regime: waveguiding properties

After fabrication, the optical guiding properties of all waveguides are investigated experimentally based on an end-facet coupling arrangement at a wavelength of 1064 nm (using a linearly polarized continuous-wave solid-state laser), corresponding to the lasing wavelength of Nd:YAG waveguides. In order to obtain systematical and thorough information of polarization dependency of guiding properties, the all-angle light transmission of each waveguide and corresponding propagation loss are measured via adjusting the excitation laser polarization at a fixed launched power, as summarized in Table 1. It should be noted that the transmitted light through the guiding structure preserves the original polarization. According to the seemingly miscellaneous data points, three key features of the Nd:YAG cladding waveguides fabricated in this work can be summarized as follows.

(A) Waveguide structures with larger sizes exhibit lower optical propagation losses. This applies to both standard cladding and modified cladding (with "ear-like" structures) waveguides. This result is quite reasonable since the primary source of propagation loss (in the form of scattering loss) is the imperfect waveguide boundary area defined by FsLDW. Such a rough boundary acts as a scattering region that has a stronger impact on the optical guiding, in contrast to larger-size waveguide structures, of more compact waveguide structures. In general, it is very difficult to completely avoid the scattering loss originated from FsLDW-induced boundary only by optimizing FsLDW fabrication parameters.

(B) For standard FsLDW depressed-cladding waveguides (*i.e.*, WG1-WG4), optical guiding property is almost polarization-independent (*i.e.*, optical propagation loss is nearly the same

Optics EXPRESS

at 1064 nm at any transverse polarization), revealing a perfect isotropic light confinement capability. The lowest propagation loss for standard claddings is determined to be around 1.45 dB/cm (in case WG4, as indicated in Table 1).

(C) In contrast to standard cladding waveguides, the corresponding waveguides with "ear-like" structures exhibit lower propagation losses, especially along TM polarization, as indicated in Table 1. For example, WG4e has a propagation loss of 1.25 dB/cm along TE polarization while 0.99 dB/cm along TM polarization, which both are lower than that of WG4 (around 1.5 dB/cm for both TE and TM polarizations). This result is mainly attributed to the good optical confinement provided by the introduction of "ear-like" structures, offering an additional low-index layer. We believe that the effect of enhanced optical confinement of the "ear-like" structure plays a more significant role along TM polarization in all cases is identical to that in FsLDW "double-line" waveguide structures, resulting a slight optical anisotropy in the guiding property (the factor of crystalline asymmetry can be excluded since Nd:YAG has a cubic crystal structure).

Table 1. FsLDW Nd:YAG cladding waveguide propagation losses

	WG1 (WG1e)	WG2 (WG2e)	WG3 (WG3e)	WG4 (WG4e)
TE (dB/cm)	2.36 (2.15)	1.84 (1.73)	1.53 (1.47)	1.53 (1.25)
TM (dB/cm)	2.18 (1.69)	1.84 (1.49)	1.49 (1.04)	1.45 (0.99)

Fluorescence intensity maps of $^4F_{3/2} \rightarrow {}^4I_{9/2}$ emission line at 946 nm for single-cladding waveguide WG4 and "ear-like" waveguide WG4e are depicted as Figs. 1(c) and 1(d). It is obvious to see that the original optical properties of Nd:YAG bulk is preserved intactly in in the waveguide core during the process of femtosecond laser writing. However, for the laser-written tracks region, the fluorescence intensity is dropped.

3.2. Continuous wave (CW) waveguide laser

In order to investigate the laser performance of the fabricated Nd:YAG waveguides, we employ an end-face coupling arrangement similar to that in Section 3.1 but replaced the laser source by a tunable CW Ti:Sapphire laser (Coherent MBR-110) for optical pumping. The pump light is linearly polarized with a wavelength centered at 808 nm. We used a plano-convex lens ($f = 25$ mm) and a microscope objective (20×/0.40) for in- and out-coupling, respectively. The waveguide sample, the lens and the objective are placed on separate manual 3D-translation optical stages, enabling flexible adjustment of coupling condition as well as optical excitation of different waveguides by simply translating the sample or the lens laterally/vertically. In the experiment, two dielectric mirrors are butt-adhered to the in- (with a reflectivity of >99.9% at 1.06 μm and a high transmittance of 99.8% at 808 nm) and out-coupling (with a reflectivity of approximately 90% at 1.06 μm and 808 nm) end facets of the sample, forming a compact Fabry-Pérot cavity. The optical alignment for measurement of each waveguide is separately optimized in order to obtain maximum output power. The whole waveguide laser characterization setup (the inserted $SnSe_2$ thin film is used as a SA for Q-switched waveguide laser generation as discussed in the next section) is schematically illustrated in Fig. 5.

The laser modes and the pump-output power dependences (for optical pumping with TM polarization) of all the cladding waveguides are shown in Fig. 6 and Fig. 7, respectively. The central lasing wavelength is 1064 nm with a full wave at half maximum (FWHM) value of 0.8 nm (with a spectrometer resolution of 0.2 nm) for all waveguides, corresponding to the transition band $^4F_{3/2} \rightarrow {}^4I_{11/2}$ of Nd^{3+} ions [38]. It is noteworthy that the lasing performance of FsLDW Nd:YAG cladding waveguides along TE polarization remains almost the same by comparing standard cladding waveguides to their counterparts with "ear-like" structures, so the

Optics EXPRESS

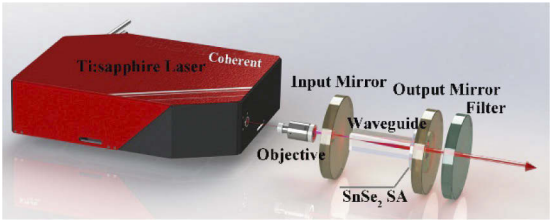

Fig. 5. Schematic diagram of Q-switched waveguide laser.

lasing performance results shown in Figs. 7(a) and 7(b) are all achieved by TM-polarized optical pumping. In particular, the pump power is detected in the light outlet of Ti:Sapphire laser. In other words, the pump power meant the launch power rather than absorbed power. Therefore, the real slope efficiency and optical-to-optical conversion efficiency should be higher than fitting values in our work. The output power is directly detected after filter. From the CW waveguide laser results, it can be found that:

(A) For cladding waveguides with radii larger than 15 μm (*i.e.*, WG3, WG4, WG3e, and WG4e), the lasing modes are more like multi-mode profile, although the "ear-like" structure is able to slightly shape the mode profile as indicated by comparing WG3 and WG3e. Nevertheless, waveguides with larger radii exhibit excellent laser performance in terms of output power (with a maximum output power of 288 mW for WG4 and 347 mW for WG4e) and slope efficiency (with a maximum slope efficiency of 31.7% for WG3 and 37.8% for WG4). The lasing threshold is < 50 mW in all cases.

(B) By comparison, the lasing performance of cladding waveguides with "ear-like" structures are superior to their standard counterparts in terms of output power (the maximum values are lifted by about 20%), slope efficiency as well as lasing threshold (for example, the lasing thresholds for WG4 and WG4e are around 40 and 10 mW, respectively), which is a reasonable result by considering the waveguide losses summarized in Table 1. With no negative impacts on lasing performance along TE polarization, the "ear-like" structure provides the distinct improvement and enhancement on both guiding properties and lasing performance in FsLDW Nd:YAG cladding waveguides for TM polarization.

(C) From the CW waveguide laser characterization, the maximum output power is determined to be 347 mW (in case of WG4e) under a pump power of 940 mW, corresponding to an optical-to-optical conversion efficiency of 36.9%. All the lasing thresholds in Fig. 6(b) are estimated to be below 10 mW. This is highly benefitted from the additional optical confinement offered by "ear-like" structures.

3.3. Q-switched waveguide laser

To investigate the saturable absorption property of $SnSe_2$ thin film as well as to further explore the lasing performance operating at pulsed regime of the fabricated waveguides, we inserted the $SnSe_2$ sample between one of the waveguide end facet and the output cavity mirror, acting as an SA for passive *Q*-switching (PQS). Besides SA, the rest of end-face coupling arrangement is remained the same as that for CW laser operation. We both realized the stable *Q*-switched operation in the Nd:YAG standard-cladding waveguide laser and ear-like waveguide laser. Figure 8 depicted the average output power of *Q*-switching operation for two kinds of waveguide structure. Caused by insertion loss from SA, the threshold pump power slightly increased and the maximum output power decreased. For "ear-like" waveguides, the average output power and slope of Q-switched

Optics EXPRESS

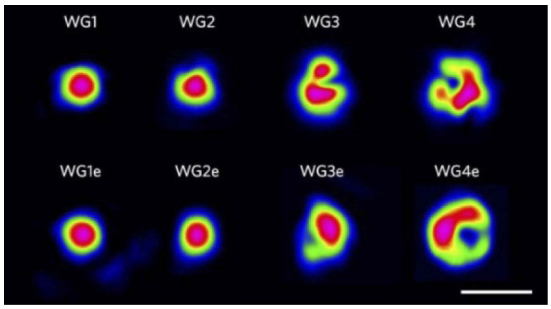

Fig. 6. Laser modes at 1.06 μm of TM polarization. The scale bar denotes 50 μm.

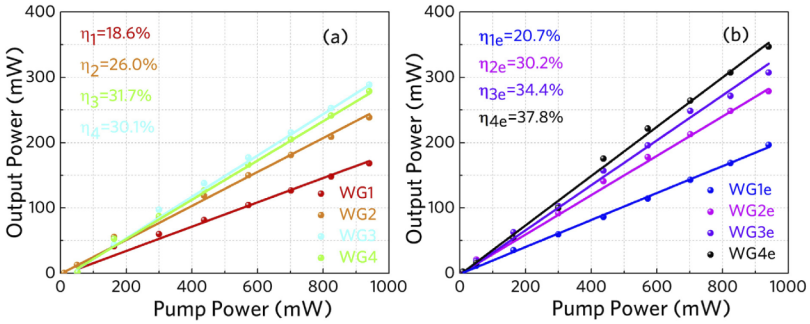

Fig. 7. Output power as a function of incident power obtained from Nd:YAG cladding waveguides at TM polarization for (a) standard cladding waveguides and (b) their counterparts with "ear-like" structures.

laser based on WG4e are highest. The value is 327 mW and 34.4%, respectively. According to the data from Figs. 8(a) and 8(b), the average output power and slope of Q-switched laser based on the "ear-like" waveguides are greatly improved compared with that of standard waveguides structure. on the whole, the variation of *Q*-switched laser performance is similar to that of CW laser in terms of laser threshold, maximum output power, slope and optical-to-optical conversion efficiency for different waveguide structures with four kinds of radius. Limited by the launched power of Ti:Sapphire laser, it is impossible to further improve the system to achieve higher output

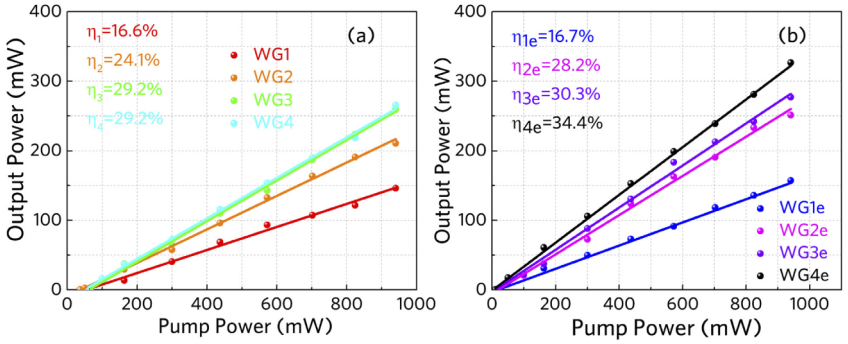

Fig. 8. Average output power of *Q*-switched operation as a function of launched power obtained from Nd:YAG cladding waveguides at TM polarization for (a) standard cladding waveguides and (b) their counterparts with "ear-like" structures.

Optics EXPRESS

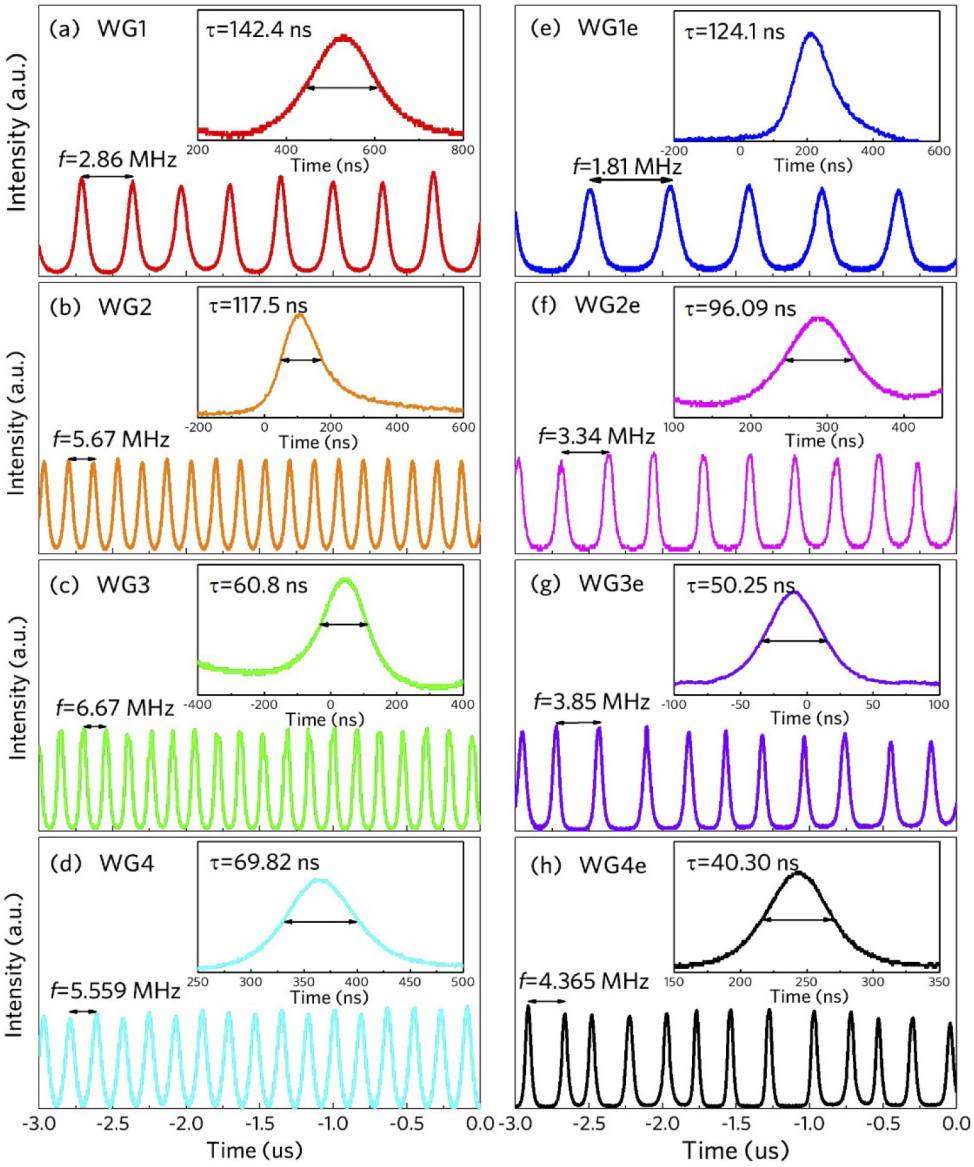

Fig. 9. Recorded pulse train of the $SnSe_2$-based Q-switched laser for (a) WG1, (b) WG2, (c) WG3, (d) WG4, (e) WG1e, (f) WG2e, (g) WG3e and (h) WG4e, respectively.

power. Nevertheless, it is noted that the relationship between the output and pump power is linear. At the high pump power, in this work, the output power does not show a saturation tendency. Therefore, it has the potential to achieve higher power if further increased launched power.

As the increase of the radius of waveguide, the pulse width tends to narrow. On the one hand, larger waveguide radius demonstrated the highest overlap of the pump beam and the waveguide modal profiles. On the other hand, the depressed-cladding waveguide geometry with an "ear-like" structure have lower propagation loss. Therefore, WG4e shows the highest efficiencies and shortest pulse width among the investigated waveguides, as shown as Fig. 9. We believe the 40.3 ns pulse to be the shortest one ever reported for the passively *Q*-switched laser using $SnSe_2$ SAs [31,39–41]. We summarize the pulsed parameters of *Q*-switched laser based

Optics EXPRESS

on the standard-cladding waveguide and cladding waveguide with "ear" structure. The results are listed in Table 2. The maximum single pulse energy is calculated to be 86.7, 75.2, 73.0 and 74.8 nJ for WG1e, WG2e, WG3e and WG4e, respectively. In the passively Q-switched lasers based on the standard cladding waveguide structure with four kinds of sizes, the maximum single pulse energy is 51.1 (WG1), 37.2 (WG2), 38.9 (WG3) and 47.8 nJ (WG4), respectively. It is obvious that a single pulse energy of Q-switching has been improved significantly for the ear-like waveguide laser.

Table 2. Q-switched laser performance summarized from Fig. 9

	WG1 (WG1e)	WG2 (WG2e)	WG3 (WG3e)	WG4 (WG4e)
Pulse Width (ns)	142.4 (124.1)	117.5 (96.09)	60.8 (50.25)	69.82 (40.30)
Repetition Rate (MHz)	2.86 (1.81)	5.67 (3.34)	6.67 (3.85)	5.56 (4.37)

4. Summary

In conclusion, the ear-like structure of depressed cladding waveguides in Nd:YAG crystal have been fabricated by direct femtosecond laser writing. From the CW and PQS laser performance analysis, the propagation loss of cladding waveguide has been significantly reduced along TM polarization, which proved depressed-cladding waveguide geometry with an "ear-like" structure really strengthen the optical confinement. Based on $SnSe_2$ SA with strong saturable absorption, a megahertz *Q*-switched laser have been established. This work throwed a new light into the femtosecond laser writing technique and proving a novel waveguide design for developing near-infrared integrated photonic devices.

Funding. National Natural Science Foundation of China (12074223, 61775120); China Postdoctoral Science Foundation (2020M682155); Qilu Young Scholar Program; Taishan Scholar Foundation of Shandong Province; Consejería de Educación, Junta de Castilla y León (SA287P18, SA136P20); Ministerio de Economía y Competitividad (FIS2017-87970R).

Acknowledgments. The authors gratefully acknowledge fruitful discussions with Q. Lu.

Disclosures. The authors declare no conflicts of interest.

References

1. E. A. J. Marcatili and R. A. Schmeltzer, "Hollow metallic and dielectric waveguides for long distance optical transmission and lasers," Bell Syst. Tech. J. **43**(4), 1783–1809 (1964).
2. C. Grivas, "Optically pumped planar waveguide lasers, Part I: Fundamentals and fabrication techniques," Prog. Quantum Electron. **35**(6), 159–239 (2011).
3. C. Grivas, "Optically pumped planar waveguide lasers: Part II: Gain media, laser systems, and applications," Prog. Quantum Electron. **45-46**, 3–160 (2016).
4. J. I. Mackenzie, J. W. Szela, S. J. Beecher, T. L. Parsonage, R. W. Eason, and D. P. Shepherd, "Crystal Planar Waveguides, a Power Scaling Architecture for Low-Gain Transitions," IEEE J. Sel. Top. Quantum Electron. **21**(1), 380–389 (2015).
5. C. Wieschendorf, J. Firth, L. Silverstri, S. Gross, F. Ladouceur, M. J. Withford, D. J. Spence, and A. Fuerbach, "Compact integrated actively Q-switched waveguide laser," Opt. Express **25**(3), 1692–1701 (2017).
6. E. Kifle, P. Loiko, C. Romero, J. R. V. de Aldana, M. Aguiló, F. Díaz, P. Camy, U. Griebner, V. Petrov, and X. Mateos, "Watt-level ultrafast laser inscribed Thulium waveguide lasers," Prog. Quantum Electron. **72**, 100266 (2020).
7. E. Kifle, P. Loiko, J. R. V. de Aldana, C. Romero, V. Llamas, J. M. Serres, M. Aguiló, F. Díaz, L. Z. Zhang, Z. B. Lin, H. F. Lin, G. Zhang, V. Zakharov, A. Veniaminov, V. Petrov, U. Griebner, X. Mateos, L. Wang, and W. D. Chen, "Low-loss fs-laser-written surface waveguide lasers at >2 μm in monoclinic Tm^{3+}:$MgWO_4$," Opt. Lett. **45**(14), 4060–4063 (2020).
8. D. G. Lancaster, S. Gross, A. Fuerbach, H. E. Heidepriem, T. M. Monro, and M. J. Withfor, "Versatile large-mode-area femtosecond laser-written Tm:ZBLAN glass chip lasers," Opt. Express **20**(25), 27503–27509 (2012).
9. Y. C. Jia and F. Chen, "Compact solid-state waveguide lasers operating in the pulsed regime: a review [Invited]," Chin. Opt. Lett. **17**(1), 012302 (2019).
10. A. Okhrimchuk, "Femtosecond fabrication of waveguides in ion-doped laser crystal," in *Coherence and Ultrashort Pulse Laser Emission*, F. J. Duarte, ed., (InTech, 2010). Available from: http://www.intechopen.com/articles/show/title/femtosecond-fabrication-of-waveguides-in-ion-doped-lasercrystals.

Optics EXPRESS

11. K. M. Davis, K. Miura, N. Sugimoto, and K. Hirao, "Writing waveguides in glass with a femtosecond laser," Opt. Lett. **21**(21), 1729–1731 (1996).
12. N. Pavel, G. Salamu, F. Voicu, F. Jipa, and M. Zamfirescu, "Diode-laser pumping into the emitting level for efficient lasing of depressed cladding waveguides realized in Nd:YVO_4 by the direct femtosecond-laser writing technique," Opt. Express **22**(19), 23057–23065 (2014).
13. D. Choudhury, J. R. Macdonald, and A. K. Kar, "Ultrafast laser inscription: perspectives on future integrated applications," Laser Photonics Rev. **8**(6), 827–846 (2014).
14. S. Gross and M. J. Withford, "Ultrafast-laser-inscribed 3D integrated photonics: challenges and emerging applications," Nanophotonics **4**(3), 332–352 (2015).
15. G. Y. Chen, F. Piantedosi, D. Otten, Q. Y. Kang, W. Q. Zhang, X. Zhou, T. M. Monro, and D. G. Lancaster, "Femtosecond-laser-written Microstructured Waveguides in BK7 Glass," Sci. Rep. **8**(1), 10377 (2018).
16. Y. C. Jia, S. X. Wang, and F. Chen, "Femtosecond laser direct writing of flexibly configured waveguide geometries in optical crystals: fabrication and application," Opto-Electron. Adv. **3**(10), 190042 (2020).
17. F. Chen and J. R. V. de Aldana, "Optical waveguides in crystalline dielectric materials produced by femtosecond-laser micromachining," Laser Photonics Rev. **8**(2), 251–275 (2014).
18. Y. C. Jia, R. Y. He, J. R. V. de Aldana, H. L. Liu, and F. Chen, "Femtosecond laser direct writing of few-mode depressed-cladding waveguide lasers," Opt. Express **27**(21), 30941–30951 (2019).
19. C. Romero, J. G. Ajates, F. Chen, and J. R. V. de Aldana, "Fabrication of Tapered Circular Depressed-Cladding Waveguides in Nd:YAG Crystal by Femtosecond-Laser Direct Inscription," Micromachines **11**(1), 10 (2020).
20. A. G. Okhrimchuk, A. V. Shestakov, I. Khrushchev, and J. Mitchell, "Depressed cladding, buried waveguide laser formed in a YAG:Nd^{3+} crystal by femtosecond laser writing," Opt. Lett. **30**(17), 2248–2250 (2005).
21. G. Croitoru and N. Pavel, "Passive Q-switching by Cr^{4+}:YAG saturable absorber of buried depressed-cladding waveguides obtained in Nd-doped media by femtosecond laser beam writing," Materials **11**(9), 1689 (2018).
22. A. G. Okhrimchuk, V. Mezentsev, A. Shestakov, and L. Bennion, "Low loss depressed cladding waveguide inscribed in YAG:Nd single crystal by femtosecond laser pulses," Opt. Express **20**(4), 3832–3843 (2012).
23. H. D. Nguyen, A. Rodenas, J. R. V. de Aldana, J. Martinez, F. Chen, M. Aguilo, M. C. Pujol, and F. Diaz, "Heuristic modelling of laser written mid-infrared $LiNbO_3$ stressed-cladding waveguides," Opt. Express **24**(7), 7777–7791 (2016).
24. Y. C. Jia, J. R. V. de Aldana, and F. Chen, "Efficient waveguide lasers in femtosecond laser inscribed double-cladding waveguides of Yb:YAG ceramics," Opt. Mater. Express **3**(5), 645–650 (2013).
25. S. Y. Choi, T. Calmano, M. H. Kim, D. Yeom, C. Kränkel, G. Huber, and F. Rotermund, "Q-switched operation of a femtosecond-laser-inscribed Yb:YAG channel waveguide laser using carbon nanotubes," Opt. Express **23**(6), 7999–8005 (2015).
26. M. H. Kim, T. Calmano, S. Y. Choi, B. J. Lee, I. H. Baek, K. J. Ahn, D. I. Yeom, C. Kränkel, and F. Rotermund, "Monolayer graphene coated Yb:YAG channel waveguides for Q-switched operation," Opt. Express **6**(8), 2468–2474 (2016).
27. R. Mary, G. Brown, S. J. Beecher, F. Torrisi, S. Milana, D. Popa, T. Hasan, Z. P. Sun, E. Lidorikis, S. Ohara, A. C. Ferrari, and A. K. Kar, "1.5 GHz picosecond pulse generation from a monolithic waveguide laser with a graphene-film saturable output coupler," Opt. Express **21**(7), 7943–7950 (2013).
28. Y. Ren, G. Brown, R. Mary, G. Demetriou, D. Popa, F. Torrisi, A. C. Ferrari, F. Chen, and A. K. Kar, "7.8-GHz Graphene-Based 2 μm Monolithic Waveguide Laser," IEEE J. Sel. Top. Quantum Electron. **21**(1), 395 (2015).
29. A. G. Okhrimchuk and P. A. Obraztsov, "11-GHz waveguide Nd:YAG laser CW mode-locked with single-layer graphene," Sci. Rep. **5**(1), 11172 (2015).
30. J. Gonzalez and I. Oleynik, "Layer-dependent properties of SnS2 and SnSe2 novel two-dimensional materials," Phys. Rev. B **94**(12), 125443 (2016).
31. C. Cheng, Z. Li, N. Dong, J. Wang, and F. Chen, "Tin diselenide as a new saturable absorber for generation of laser pulses at 1 μm," Opt. Express **25**(6), 6132–6140 (2017).
32. K. P. Wang, J. Wang, J. T. Fan, A. Lotya, and W. J. Blau, "Ultrafast Saturable Absorption of Two-Dimensional MoS_2 Nanosheets," ACS Nano **7**(10), 9260–9267 (2013).
33. K. P. Wang, Y. Y. Feng, C. X. Chang, J. X. Zhan, and J. Wang, "Broadband ultrafast nonlinear absorption and nonlinear refraction of layered molybdenum dichalcogenide semiconductors," Nanoscale **6**(18), 10530–10535 (2014).
34. A. Shafique, A. Samad, and Y. H. Shin, "Ultra low lattice thermal conductivity and high carrier mobility of monolayer SnS_2 and $SnSe_2$: a first principles study," Phys. Chem. Chem. Phys. **19**(31), 20677–20683 (2017).
35. G. R. Castillo, C. Romerao, G. Lifante, D. Jaque, F. Chen, O. Varela, E. G. Garcia, C. Mendez, S. C. Lopez, and J. R. V. de Aldana, "Stress-induced waveguides in Nd:YAG by simultaneous double-beam irradiation with femtosecond pulses," Opt. Mater. **51**, 84–88 (2016).
36. M. Liu, Y. Shi, M. M. Wu, Y. Tian, H. N. Wei, Q. Q. Sun, M. Shafi, and B. Y. Man, "UV surface-enhanced Raman scattering properties of $SnSe_2$ nanoflakes," J. Raman Spectrosc. **51**(5), 750–755 (2020).
37. J. Wang, B. Gu, H. T. Wang, and X. W. Ni, "Z-scan analytical theory for material with saturable absorption and two-photon absorption," Opt. Commun. **283**(18), 3525–3528 (2010).
38. V. Lupei and N. Pavel, "Laser emission in highly doped Nd:YAG crystals under $^4F_{5/2}$ and $^4F_{3/2}$ pumping," Opt. Lett. **26**(21), 1678–1680 (2001).

Optics EXPRESS

39. X. Q. Liu, Q. Yang, C. H. Zuo, Y. P. Cao, X. L. Lun, P. C. Wang, and X. Y. Wang, "2 μm passive Q-switched Tm:YAP laser with $SnSe_2$ absorber," Opt. Eng. **57**(12), 1 (2018).
40. Q. Song, B. Y. Zhang, and G. J. Wang, "Characterization of $SnSe_2$ saturable absorber by THz-TDS and used in dual-wavelength passively Q-switched laser," Optik **174**, 35–39 (2018).
41. R. Y. Sun, H. N. Zhang, and N. N. Xu, "High-power passively Q-switched Yb-doped fiber laser based on Tin selenide as a saturable absorber," Laser Phys. **28**(8), 085105 (2018).